



Pyrolyzed polydopamine-modified carbon black for selective and durable electrocatalytic oxygen reduction to hydrogen peroxide in acidic medium

Dan Wang^a, Sitan Li^a, Xiaoxin Zhang^b, Bo Feng^a, Yan Pei^a, Yunfeng Zhu^c, Wei Xu^c, Zhen-Hua Li^a, Minghua Qiao^{a,*}, Baoning Zong^{b,*}

^a Collaborative Innovation Center of Chemistry for Energy Materials, Department of Chemistry and Shanghai Key Laboratory of Molecular Catalysis and Innovative Materials, Fudan University, Shanghai 200438, PR China

^b State Key Laboratory of Catalytic Materials and Chemical Engineering, Research Institute of Petroleum Processing, SINOPEC, Beijing 100083, PR China

^c State Key Laboratory of Safety and Control for Chemicals, SINOPEC Research Institute of Safety Engineering, Qingdao, Shandong 266101, PR China

ARTICLE INFO

Keywords:

Hydrogen peroxide
Dopamine
Carbon black
Electrocatalysis
Oxygen reduction reaction

ABSTRACT

Electrochemical production of H₂O₂ from O₂ via the two-electron reaction pathway (2e-ORR) is a promising alternative to the energy- and organic pollutant-intensive industrial anthraquinone process. However, irrespective of numerous research efforts on catalyst design and remarkable advances made in this area, the catalysts displaying high H₂O₂ production rate so far unexceptionally required expensive/hazardous catalyst precursors and involved tedious steps and/or harsh treating conditions. Herein, we report a slightly nitrogen-doped carbon 2e-ORR catalyst that was synthesized simply by pyrolyzing a polydopamine (PDA) coating on Vulcan XC72 carbon black (p-PDA/XC). In H₂O₂ production via ORR in an acidic electrolyte, the catalyst showed 185 mV less overpotential than XC and remarkably high selectivity up to 96%. Highly efficient and durable H₂O₂ production was demonstrated by the stable accumulation of H₂O₂ to 1368 mmol g_{cat}⁻¹ within 8 h, translating to a H₂O₂ production rate of 171 mmol g_{cat}⁻¹ h⁻¹. A good linear relationship was identified between the H₂O₂ partial current and the surface content of the C–O/C–N and C=O species for the XC and p-PDA/XC catalysts, inferring that the C atoms in or adjacent to these species serve as the active sites for 2e-ORR to H₂O₂. The inexpensive starting materials, facile synthetic strategy, and excellent catalytic performance of the p-PDA/XC catalyst may accelerate the establishment of an affordable, safe, and direct O₂-to-H₂O₂ electrochemical process.

1. Introduction

Hydrogen peroxide (H₂O₂), an important and widely used green oxidant, is nowadays mainly produced by the anthraquinone process that is constituted by four steps: hydrogenation, oxidation, H₂O₂ extraction, and working solution recovery [1]. Aside from the lengthy process flow, the use of heavy aromatics and esters as the solvent and the gradual degradation of expensive anthraquinone make the anthraquinone process highly polluting and costly [2–4]. Electrocatalytic production of H₂O₂ via the oxygen reduction reaction (ORR) under H₂-free and room temperature conditions shows promise for the development of an affordable, clean, safe, and decentralized process [5–11]. However, the ORR reaction can occur in two pathways, i.e., the two-electron pathway (2e-ORR) to H₂O₂ and the four-electron pathway (4e-ORR) to H₂O [12–18]. As a competing reaction for H₂O₂ production, the 4e-ORR pathway is thermodynamically more favored [19]. Moreover, H₂O₂ may

undergo further two-electron reduction to produce the unwanted H₂O. To suppress the excessive reduction of O₂ and improve the selectivity to H₂O₂, the development of electrocatalysts with active sites specific for 2e-ORR is a central task.

Carbon-based nanomaterials are desirable catalysts/catalyst precursors for electrocatalysis because of their earth-abundance, high electrical conductivity, and excellent chemical robustness [20]. In principle, the electrocatalytic activity and selectivity for H₂O₂ production over the carbon-based nanomaterials can be improved by finely tuning their geometric [21–24] and electronic structures [25,26]. Moreover, unlike the noble metal- and transition metal-based materials [27,28] that are vulnerable to acid corrosion and thus can only work stably in basic or neutral electrolytes, the metal-free carbon-based nanomaterials are acid-proof, thus ideally suitable for 2e-ORR in acidic electrolytes. It has the following advantages to produce H₂O₂ in acidic medium: (1) H₂O₂ is unstable in basic medium and tends to decompose

* Corresponding authors.

E-mail addresses: mhqiao@fudan.edu.cn (M. Qiao), zongbn.ripp@sinopec.com (B. Zong).

<https://doi.org/10.1016/j.apcatb.2021.121036>

Received 12 October 2021; Received in revised form 3 December 2021; Accepted 20 December 2021

Available online 23 December 2021

0926-3373/© 2021 Elsevier B.V. All rights reserved.

[29]; Instead, H_2O_2 is stable in acidic medium [30]; and (2) H_2O_2 is more oxidizing in acidic or neutral medium than in basic medium [31]. However, irrespective of numerous research efforts on catalyst design and remarkable advances made in this area, the carbon-based catalysts displaying high H_2O_2 production rate in acidic electrolytes reported so far unexceptionally required expensive/hazardous catalyst precursors and involved tedious steps and/or harsh treating conditions [32–34]. It is highly desirable to develop a high-performance carbon-based catalyst for 2e-ORR in acid electrolyte using economical precursors and facile synthetic strategies.

Dopamine, a nitrogenous natural chemical, shows superior adhesion arising from its catechol and amine groups. Messersmith and co-workers discovered that dopamine can spontaneously polymerize in alkaline solution such as ammonia in air to form a polydopamine (PDA) coating on virtually any substrate [35]. After pyrolysis, PDA can be transformed into a N-doped carbon layer, which modifies the surface hydrophilicity and electronic property of the substrate [36,37]. In light of the interesting characteristics of dopamine, herein we designed and successfully synthesized the N-doped carbon catalysts simply by pyrolyzing the PDA coating on the Vulcan XC72 carbon black (p-PDA/XC). The loading of PDA was manipulated by varying the volume of ammonia during dopamine polymerization. At the optimal loading of PDA, the catalyst displayed advantageous 2e-ORR activity and superior H_2O_2 selectivity. Moreover, the catalyst afforded a stable and high H_2O_2 production rate for at least 8 h in acidic electrolyte, making p-PDA/XC a highly potential candidate for the large-scale decentralized production of H_2O_2 from O_2 .

2. Experimental

2.1. Chemicals

Vulcan XC72 carbon black (abbreviated as XC) was purchased from Cabot. Dopamine hydrochloride was purchased from Aladdin Reagent. Ammonia (28–30 wt%) and anhydrous ethanol were purchased from Sinopharm Chemical Reagent. Nafion, isopropanol, and HClO_4 were purchased from Sigma-Aldrich. All chemicals were used without further purification. N_2 and O_2 were purchased from Shanghai TOMOE Gases.

2.2. Preparation

Scheme 1 illustrates the facile dopamine polymerization/coating–pyrolysis strategy for the synthesis of the p-PDA/XC catalysts. XC (500 mg), ammonia (1, 2, 5, and 7 mL), deionized (DI) water (45 mL), and ethanol (20 mL) were added in a round-bottomed flask and stirred for 0.5 h at room temperature. Dopamine hydrochloride (250 mg) was added and stirred at room temperature for 48 h. The resulting suspension was filtered and dried at 80 °C. The dried powders, denoted as PDA₁/XC, PDA₂/XC, PDA₅/XC, and PDA₇/XC, in which the subscript corresponds to the volume of ammonia, were heated to 400 °C at a ramping rate of 2 °C min^{−1} under N_2 flow and maintained for 1 h. The temperature was then raised to 800 °C at a ramping rate of 5 °C min^{−1} and maintained for 3 h for further pyrolysis. The obtained black materials were denoted as p-PDA₁/XC, p-PDA₂/XC, p-PDA₅/XC, and p-PDA₇/XC, where *p* represents pyrolysis. XC was also calcined at 800 °C for 3 h

under N_2 flow at a ramping rate of 5 °C min^{−1} prior to characterization and activity testing.

We found that the amount of PDA coated on XC can be manipulated by the volume of ammonia as the preparation variable. As demonstrated in Fig. S1, the masses of both the dried and the pyrolyzed PDA/XC nanocomposites were negatively correlated with the volume of ammonia, i.e., the less the volume of ammonia, the more is the amount of PDA coated on XC. This dependence can be explained by the slightly negative Zeta potential of Vulcan XC72 (−15.8 mV, Fig. S2), which electrostatically attracts the protonated dopamine in dopamine hydrochloride. With the increase in the volume of ammonia, more protonated dopamine molecules are transformed to the electrically neutral dopamine, thus decreasing the amount of dopamine deposited on XC for successive polymerization.

For comparison, the self-standing pyrolyzed PDA₁ (p-PDA₁) was prepared as follows. Ammonia (1 mL), DI water (45 mL), and ethanol (20 mL) were added in the round-bottomed flask. Then the mixture was stirred at room temperature for 0.5 h. Dopamine hydrochloride (250 mg) was added and stirred at room temperature for 48 h. The resulting suspension was filtered and dried at 80 °C. The dried powders were heated to 400 °C at a ramping rate of 2 °C min^{−1} under N_2 flow and maintained for 1 h. The temperature was subsequently raised to 800 °C at a ramping rate of 5 °C min^{−1} and maintained for 3 h for further pyrolysis.

2.3. Characterization

Zeta potential was determined on a Zetasizer Nano-ZS90 analyzer (Malvern Instruments). The solution for zeta potential measurement was prepared by dispersing Vulcan XC72 carbon black into DI water and analyzed at room temperature.

Transmission electron microscopic (TEM) and energy dispersive spectroscopic (EDS) characterizations were conducted on a FEI Tecnai G2S-Twin F20 field-emission scanning transmission electron microscope with an Oxford Instrument X-Max 80 T EDS detector. Elemental analysis was conducted on elemental vario MICRO CUBE spectrometer.

Powder X-ray diffraction (XRD) patterns were collected on a Bruker AXS D8 Advance X-ray diffractometer using Ni-filtered $\text{Cu K}\alpha$ radiation equipped with a LynxEye 1-dimensional linear Si strip detector.

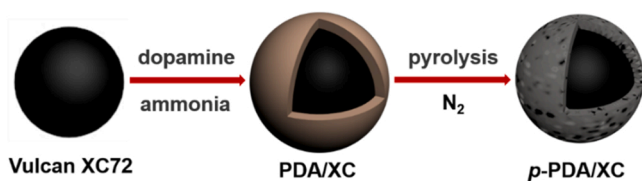
N_2 adsorption–desorption isotherm was acquired on a Micromeritics ASAP 2020 Plus system at −196 °C. Before measurement, the material was degassed in vacuo at 300 °C for 10 h to remove the adventitious contaminants. The Brunauer–Emmett–Teller (BET) method and DFT equation were applied to obtain the specific surface areas and pore size distribution, respectively.

Raman spectrum was collected on a Horiba Jobin Yvon XploRA microRaman spectrometer with 10 mW of power and 532 nm of the wavelength of the laser source. The spectrum was recorded at room temperature in the 80–3600 cm^{−1} range with the spectral resolution of ca. 1.8 cm^{−1}. The acquisition time was 30 s. The surface chemical state and surface composition were determined by X-ray photoelectron spectroscopy (XPS) on a Thermo ESCALAB 250Xi system with a monochromatic Al $\text{K}\alpha$ excitation source.

Electrochemical capacitance measurement was used to determine the electrochemical active surface area (ECSA) of the catalyst. The electrochemical double-layer capacitance was determined from the cyclic voltammetry (CV) curves measured in a potential range without redox processes according to the equation:

$$C_{dl} = j_c/v$$

where C_{dl} , j_c , and v are the double-layer capacitance (F cm^{−2}) of the catalyst, charging current density (mA cm^{−2}), and scan rate (mV s^{−1}), respectively. The CV curves were measured in a potential range of 0.70–0.80 V devoid of the redox processes in N_2 -saturated 0.1 M HClO_4 at the scan rates of 5, 10, 15, 20, and 25 mV s^{−1}. The obtained capacitive



Scheme 1. Illustration of the dopamine polymerization/coating–pyrolysis strategy for the synthesis of the p-PDA/XC catalysts. The amount of the PDA coating can be controllably adjusted by changing the volume of ammonia.

currents were plotted against the scan rate. The C_{dl} was derived from the linear fit. The specific capacitance can be converted into ECSA using the specific capacitance value of a standard with known ECSA. However, such a standard is difficult to obtain, so the C_{dl} was directly used to represent ECSA.

2.4. Electrocatalytic testing

Electrocatalytic testing was conducted on a CH Instruments CHI760E electrochemical workstation and a PINE Instruments AFMSRCE rotator. The three-electrode arrangement was employed, with a rotating ring disk electrode (RRDE) including a glassy carbon disk (0.247 cm^2) as the working electrode and a Pt ring (0.186 cm^2) to collect the H_2O_2 partial current, a reversible hydrogen electrode (RHE) as the reference electrode, and a graphite rod as the counter electrode. The working electrode was polished with $0.3\text{ }\mu\text{m}$ corundum aqueous suspension for 5 min and $0.05\text{ }\mu\text{m}$ corundum aqueous suspension for 5 min, and ultrasonicated in DI water for 30 s. The catalyst ink was prepared by mixing 2 mg of catalyst, 0.3 mL of DI water, 0.05 mL of 5% Nafion, and 0.15 mL of isopropanol and ultrasonicated for at least 1 h. Ten μL of the aliquot was dripped onto the glassy disk electrode and dried naturally at room temperature.

Prior to the electrocatalytic testing, cyclic voltammetry (CV) was performed to clean the catalyst-loaded disk electrode and the Pt ring electrode separately in the N_2 -saturated 0.1 M HClO_4 electrolyte between 0 and 1.2 V (vs. RHE, the same below) at a scan rate of 50 mV s^{-1} for 20 cycles, at which steady CV responses were obtained. Thereafter, the background current was determined by collecting the CV curves by sweeping the potential between 0 and 1.0 V at a scan rate of 50 mV s^{-1} in the N_2 -saturated 0.1 M HClO_4 electrolyte. Subsequently, O_2 was bubbled into the 0.1 M HClO_4 electrolyte for 0.5 h to saturate the electrolyte and kept on bubbling throughout the reaction. The ORR activity was investigated by CV in the range of 1.0–0 V at a scan rate of 50 mV s^{-1} . The occurrence of the ORR reaction on the $p\text{-PDA/XC}$ catalysts was confirmed by the progressively increased reduction current with the lowering of the potential in the O_2 -saturated 0.1 M HClO_4 electrolyte. In contrast, only a rectangular voltammogram with no redox peaks was recorded in the N_2 -saturated 0.1 M HClO_4 electrolyte (Fig. S3).

The catalytic activity and selectivity to H_2O_2 were assessed by linear sweep voltammetry (LSV) from 1.0 to 0 V on the RRDE at a scan rate of 10 mV s^{-1} and a rotation speed of 1600 rpm in the O_2 -saturated 0.1 M HClO_4 electrolyte with O_2 bubbling throughout the reaction. The total current (i_d) was measured on the catalyst-loaded disk electrode. During LSV, the Pt ring electrode was potentiostated at 1.2 V to allow for the oxidation of H_2O_2 while avoiding the ORR reaction. Therefore, the ring current (i_r) was equivalent to the H_2O_2 partial current, which enabled the quantification of H_2O_2 . The onset potential was defined as the potential corresponding to 0.01 mA cm^{-2} of the H_2O_2 partial current density ($j(\text{H}_2\text{O}_2)$) [38]. The H_2O_2 selectivity, i.e., the percentage of O_2 converted to H_2O_2 , was calculated using the following equation:

$$\text{H}_2\text{O}_2\% = \frac{2}{1 + \frac{i_r}{N \times i_d}} \times 100$$

where i_r , i_d , and N denote the ring current, disk current, and collection efficiency (37%), respectively.

The number of electron transferred (n) at the disk electrode during ORR was calculated as:

$$n = \frac{4|i_d|}{|i_d| + \frac{i_r}{N}}$$

Chronoamperometry stability test was performed using the three-electrode catalyst test configuration by holding the potential on the rotating disk electrode (RDE, 0.196 cm^2) at 0.1 V with the rotation speed of 1600 rpm in the O_2 -saturated 0.1 M HClO_4 electrolyte. The

reaction liquid was sampled at intervals. After complexing with a $\text{TiOSO}_4/\text{H}_2\text{SO}_4$ reagent, the concentration of H_2O_2 was quantified photometrically on a Shimadzu UV-1800 UV-Vis spectrophotometer according to the Beer–Lambert law.

3. Results and discussion

3.1. Synergy between $p\text{-PDA}$ and XC in 2e-ORR

The electrocatalytic performances of the XC, $p\text{-PDA}_1$, and $p\text{-PDA}_1/\text{XC}$ catalysts in 2e-ORR to H_2O_2 were comparatively studied using LSV under identical reaction conditions and catalyst mass. In light of the polarization curves in Fig. 1a, the onset potential of the XC catalyst measured at $j(\text{H}_2\text{O}_2) = 0.01\text{ mA cm}^{-2}$ was 0.187 V, which is negative to those of the $p\text{-PDA}_1$ and $p\text{-PDA}_1/\text{XC}$ catalysts by 0.244 V and 0.185 V, respectively, reflecting that the $p\text{-PDA}$ catalyst is much more active than XC in ORR either in the free-standing or the supported form. At 0 V, the $p\text{-PDA}_1/\text{XC}$ catalyst gave the highest H_2O_2 partial current of 0.121 mA, while the H_2O_2 partial currents on the XC and $p\text{-PDA}_1$ catalysts were only about 50% and 30% of that on the $p\text{-PDA}_1/\text{XC}$ catalyst, respectively, highlighting the occurrence of the synergistic effect between $p\text{-PDA}$ and carbon black that drastically boosted the catalytic activity in electroreduction of O_2 to H_2O_2 .

Fig. 1b shows that in the range of 0.3–0 V, the H_2O_2 selectivity increased from 63.2% to 83.2% on the XC catalyst. On the $p\text{-PDA}_1$ catalyst, the H_2O_2 selectivity increased slightly from 77.8% to 80.5% in the same potential range. For the $p\text{-PDA}_1/\text{XC}$ catalyst, the H_2O_2 selectivity decreased slightly from 79.8% to 77.1%, showing that the synergy between $p\text{-PDA}_1$ and carbon black can favorably improve the selectivity at more positive potential. However, at less positive potential, a combination of $p\text{-PDA}_1$ and carbon black led to slightly lower selectivity. Therefore, the loading of $p\text{-PDA}$ was adjusted below to acquire the optimal formulation of the $p\text{-PDA/XC}$ catalyst with both enhanced activity and selectivity.

3.2. Dependence of 2e-ORR performance on $p\text{-PDA}$ loading

Fig. 2 presents the LSV curves and the derived H_2O_2 selectivity and electron transfer number over the $p\text{-PDA/XC}$ catalysts with different $p\text{-PDA}$ loadings. According to Fig. 2a, all the $p\text{-PDA/XC}$ catalysts displayed a similar onset potential of ca. 0.372 V, inferring that $p\text{-PDA}$ on carbon black generated new active sites identical in nature. On the other hand, the ORR activity was strongly contingent on the loading of $p\text{-PDA}$. Among the $p\text{-PDA/XC}$ catalysts, the $p\text{-PDA}_5/\text{XC}$ catalyst possessed the highest total current of 0.203 mA at 0 V, followed by the $p\text{-PDA}_7/\text{XC}$ (0.181 mA), $p\text{-PDA}_2/\text{XC}$ (0.160 mA), and $p\text{-PDA}_1/\text{XC}$ (0.121 mA) catalysts. As shown in Fig. 3, the Tafel slopes of the $p\text{-PDA}_1/\text{XC}$, $p\text{-PDA}_2/\text{XC}$, $p\text{-PDA}_5/\text{XC}$, and $p\text{-PDA}_7/\text{XC}$ catalysts were 196.7, 168.3, 157.1, and 162.7 mV dec^{-1} , respectively, which complies with the sequence of the total current and reflects the fastest kinetics on the $p\text{-PDA}_5/\text{XC}$ catalyst.

As presented in Fig. 2b, the H_2O_2 selectivity in the range of 0.3–0 V follows the same sequence as that of the activity for the $p\text{-PDA/XC}$ catalysts. It is remarkable that the $p\text{-PDA}_5/\text{XC}$ catalyst sustained a high H_2O_2 selectivity up to $\sim 96\%$ across a broad potential window. The average electron transfer number in the range of 0.3–0 V was ca. 2.46, 2.24, 2.09, and 2.13 for the $p\text{-PDA}_1/\text{XC}$, $p\text{-PDA}_2/\text{XC}$, $p\text{-PDA}_5/\text{XC}$, and $p\text{-PDA}_7/\text{XC}$ catalysts, respectively (Fig. 2c). These results evidence that the active sites for 2e-ORR to H_2O_2 is the most abundant on the $p\text{-PDA}_5/\text{XC}$ catalyst. Moreover, as compared in Table S1, the $p\text{-PDA}_5/\text{XC}$ catalyst is among the most selective carbon-based catalysts in 2e-ORR to H_2O_2 in acidic electrolytes.

3.3. Catalytic stability and H_2O_2 productivity

As longer catalyst lifetime benefits the techno-economics of the ORR-to- H_2O_2 technology, the catalytic stability is a key property to take into

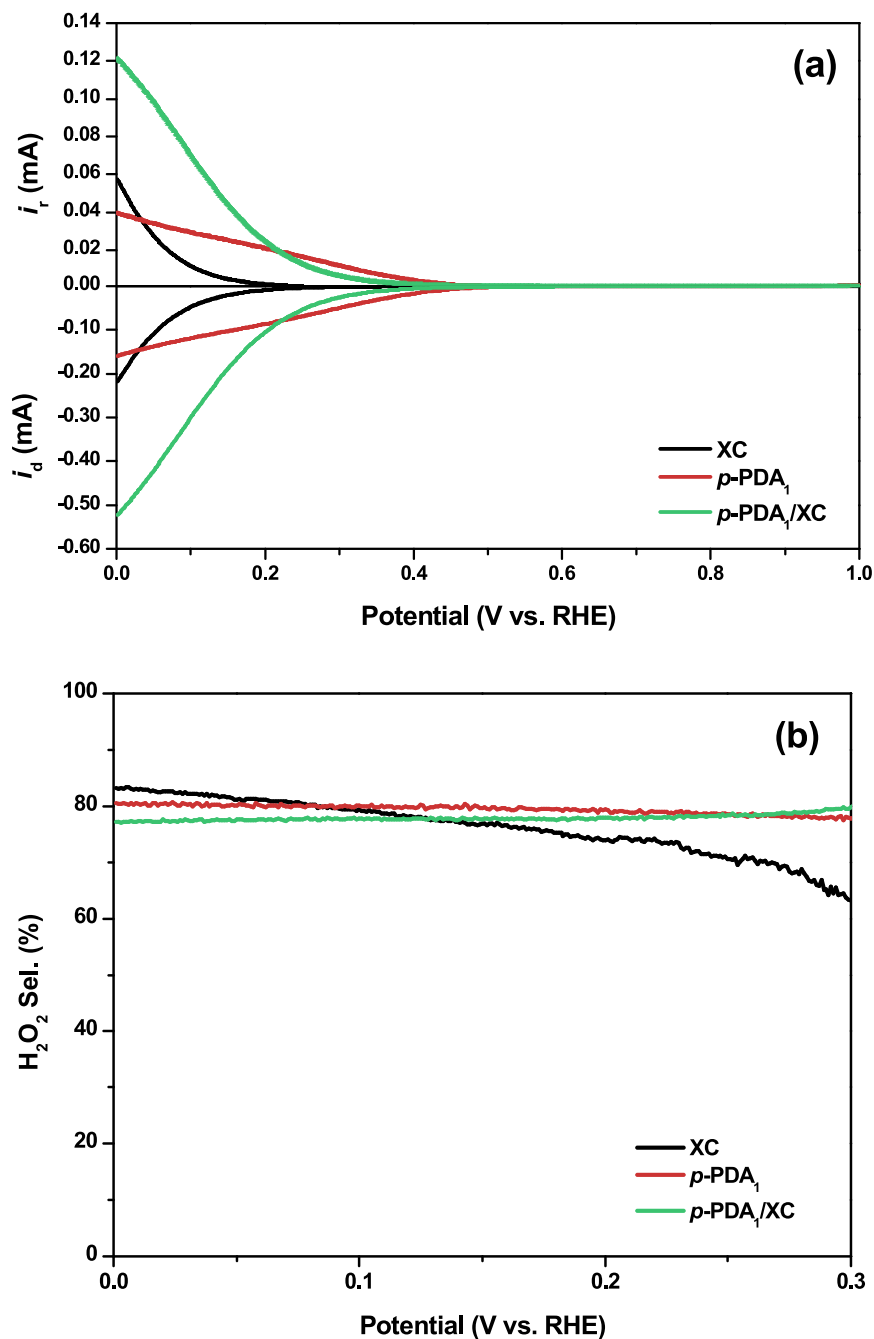


Fig. 1. RRDE ORR results of the XC, *p*-PDA₁, and *p*-PDA₁/XC catalysts in the O₂-saturated 0.1 M HClO₄ electrolyte. (a) Linear sweep voltammograms, and (b) H₂O₂ selectivity calculated from the Pt ring current in (a). Reaction conditions: 40 μg of catalyst, scan rate of 10 mV s⁻¹, and rotation speed of 1600 rpm. The Pt ring was potentiostated at 1.2 V vs. RHE for H₂O₂ detection.

account. Accelerated durability testing (ADT) has been widely used to test the cyclic stability of the catalysts, which generally involves electrochemically cycling the catalyst at rapid scan rates for a certain number of cycles [39]. ADT testing of the *p*-PDA/XC catalysts was conducted by applying 3000 cycles between 1.0 and 0 V at a scan rate of 200 mV s⁻¹. Fig. 4 shows that the CV profiles after 3000 cycles generally resembled those of the initial cycles, which denotes the good electrocatalytic stability of the *p*-PDA/XC catalysts. In particular, the *p*-PDA₅/XC catalyst exhibited the minimum decay in both onset potential and current. After 3000 CV cycles, the decay in the H₂O₂ partial current on the *p*-PDA₅/XC catalyst was less than 8%, while they were higher on the *p*-PDA₁/XC, *p*-PDA₂/XC, and *p*-PDA₇/XC catalysts as 14%, 15%, and 10%, respectively.

Since the *p*-PDA₅/XC catalyst outperformed other *p*-PDA/XC catalysts in activity, selectivity, and stability, the electrocatalytic H₂O₂ production and accumulation was tested on this catalyst by chronoamperometry. During stability testing, an aliquot of the electrolyte was sampled at intervals to obtain the real-time concentration of H₂O₂. According to Fig. 5, the concentration of H₂O₂ increased linearly with the reaction time, highlighting the stable and continuous production of H₂O₂ on the *p*-PDA₅/XC catalyst. The H₂O₂ concentration amounted to 1368 mmol g⁻¹ within 8 h, which was translated to a H₂O₂ production rate of 171 mmol g_{cat}⁻¹ h⁻¹. The excellent stability of the *p*-PDA₅/XC catalyst in H₂O₂ production was further evidenced by the stable cathodic current density at around 2.8 mA cm⁻² over 8 h. As compared in Table S2, the H₂O₂ production rate on the *p*-PDA₅/XC catalyst is

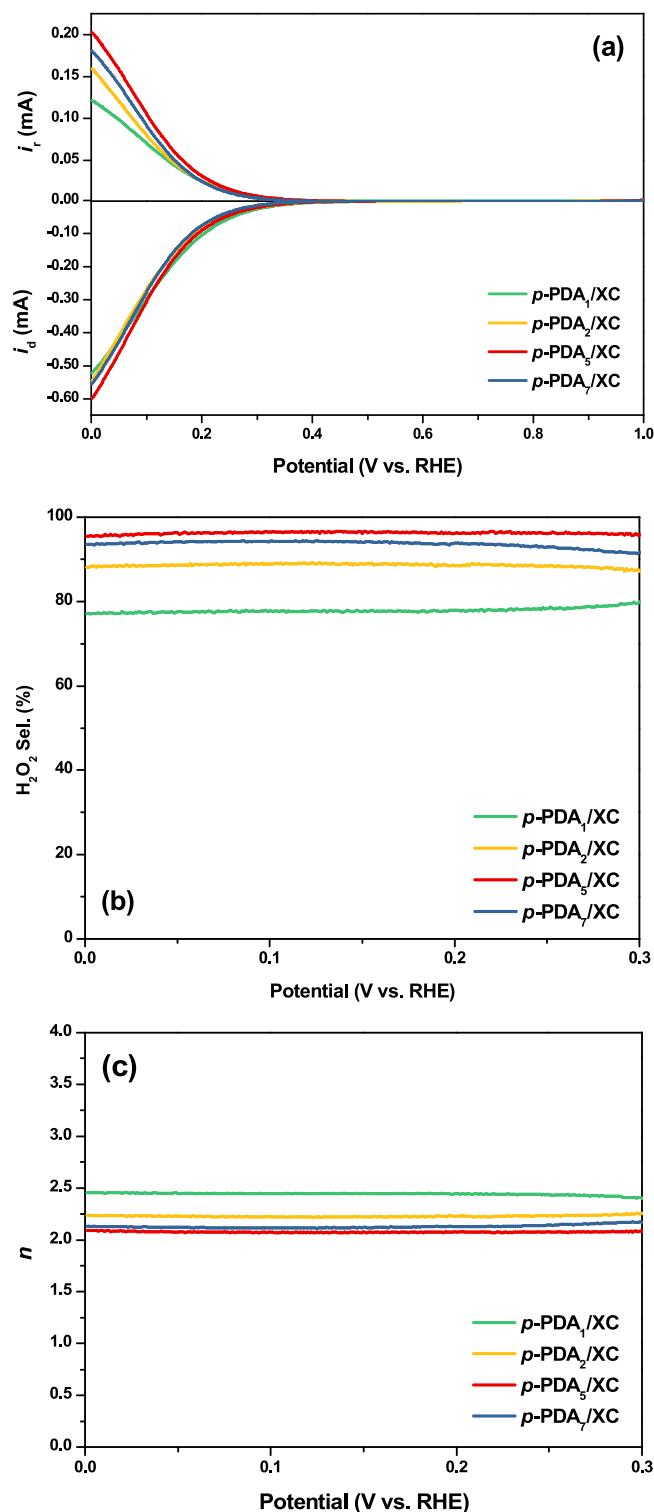


Fig. 2. RRDE ORR results of the $p\text{-PDA}/\text{XC}$ catalysts in the O_2 -saturated 0.1 M $HClO_4$ electrolyte. (a) Linear sweep voltammograms, (b) H_2O_2 selectivity calculated from the Pt ring current in (a), and (c) electron transfer number. Reaction conditions: 40 μg of catalyst, scan rate of 10 mV s^{-1} , and rotation speed of 1600 rpm. The Pt ring was potentiostated at 1.2 V vs. RHE for H_2O_2 detection.

among the highest values reported so far on the carbon-based catalysts for 2e-ORR to H_2O_2 in acidic electrolytes. As far as we are aware of, the H_2O_2 production rate on the $p\text{-PDA}_5/\text{XC}$ catalyst is only inferior to those on the HPC-H24 [32], (N)-RFC [33], and FPC-800 catalysts [34] also

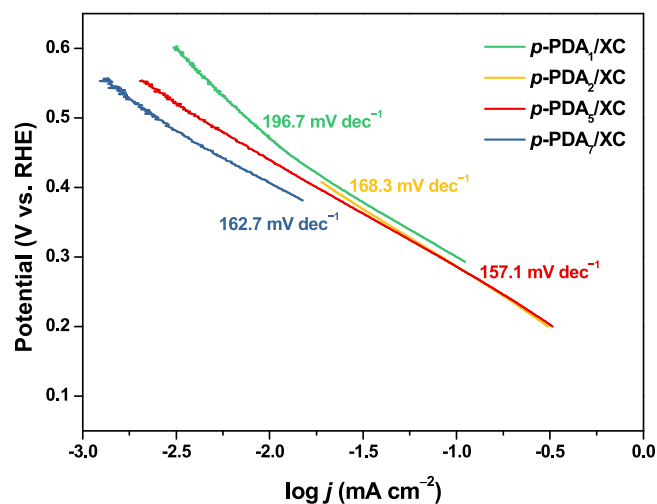


Fig. 3. Tafel slopes of the $p\text{-PDA}/\text{XC}$ catalysts in the O_2 -saturated 0.1 M $HClO_4$ electrolyte with a scan rate of 10 mV s^{-1} and a rotation speed of 1600 rpm.

evaluated in acidic electrolytes. It should be noted that the preparation of those catalysts required expensive/hazardous precursors and involved tedious steps and/or harsh treating conditions [32–34]. In contrast, the precursors for the preparation of the $p\text{-PDA}_5/\text{XC}$ catalyst are more affordable, and its preparation procedures are much simpler and safer.

3.4. Structural, compositional, and textural properties

The TEM images of XC, PDA_5/XC , and $p\text{-PDA}_5/\text{XC}$ representing the $p\text{-PDA}/\text{XC}$ catalysts at different synthetic stages are presented in Fig. 6. XC displayed the spherical morphology typical for Vulcan XC72 carbon black with the average particle diameter of 36.4 nm (Fig. 6a). PDA_5/XC also displayed the spherical morphology but with a larger particle diameter of 45.9 nm (Fig. 6b), indicating the formation of a PDA coating of ca. 4.7 nm in thickness on XC. As expected, the particle diameter of the $p\text{-PDA}_5/\text{XC}$ catalyst was shrunk to 41.1 nm (Fig. 6c) due to the pyrolysis of the PDA coating, which was still larger than that of XC. The elemental mapping images of the $p\text{-PDA}_5/\text{XC}$ catalyst show that the C, O, and N elements were homogeneously distributed on the catalyst (Fig. S4) and confirm that XC was successfully modified with $p\text{-PDA}$. Elemental analysis (Table 1) further revealed that the N content was negatively correlated with the volume of ammonia used during dopamine polymerization, with the $p\text{-PDA}_1/\text{XC}$ catalyst possessing the highest N content, followed by the $p\text{-PDA}_2/\text{XC}$, $p\text{-PDA}_5/\text{XC}$, and $p\text{-PDA}_7/\text{XC}$ catalysts. This trend also complies with the decrease in the masses of the PDA/XC and $p\text{-PDA}/\text{XC}$ samples with the increase in the volume of ammonia (Fig. S1).

The XRD patterns of the XC and $p\text{-PDA}/\text{XC}$ catalysts are shown in Fig. 7. The diffraction peaks remained at 2θ of 25° and 44° ascribable to the (002) and (100) diffractions of the graphitic carbon, respectively [40], irrespective of the coating of PDA and the experiencing of high-temperature pyrolysis. No additional diffraction peaks were resolved, which is consistent with the low loadings of N on the $p\text{-PDA}/\text{XC}$ catalysts (Table 1).

The textural properties of the XC and $p\text{-PDA}/\text{XC}$ catalysts were characterized by nitrogen physisorption. All the catalysts displayed a type I isotherm with an H4 hysteresis loop with sharp uptake at low relative pressure and unsaturated N_2 uptake at high relative pressure (Fig. 8a), manifesting the coexistence of mesoporous, macroporous, and microporous structures. The hierarchically porous structure of these catalysts is further confirmed by the pore size distributions illustrated in Fig. 8b. The S_{BET} increased from the $p\text{-PDA}_1/\text{XC}$ catalyst to the $p\text{-PDA}_5/\text{XC}$ catalyst, and then levelled off on the $p\text{-PDA}_7/\text{XC}$ catalyst (Table 1).

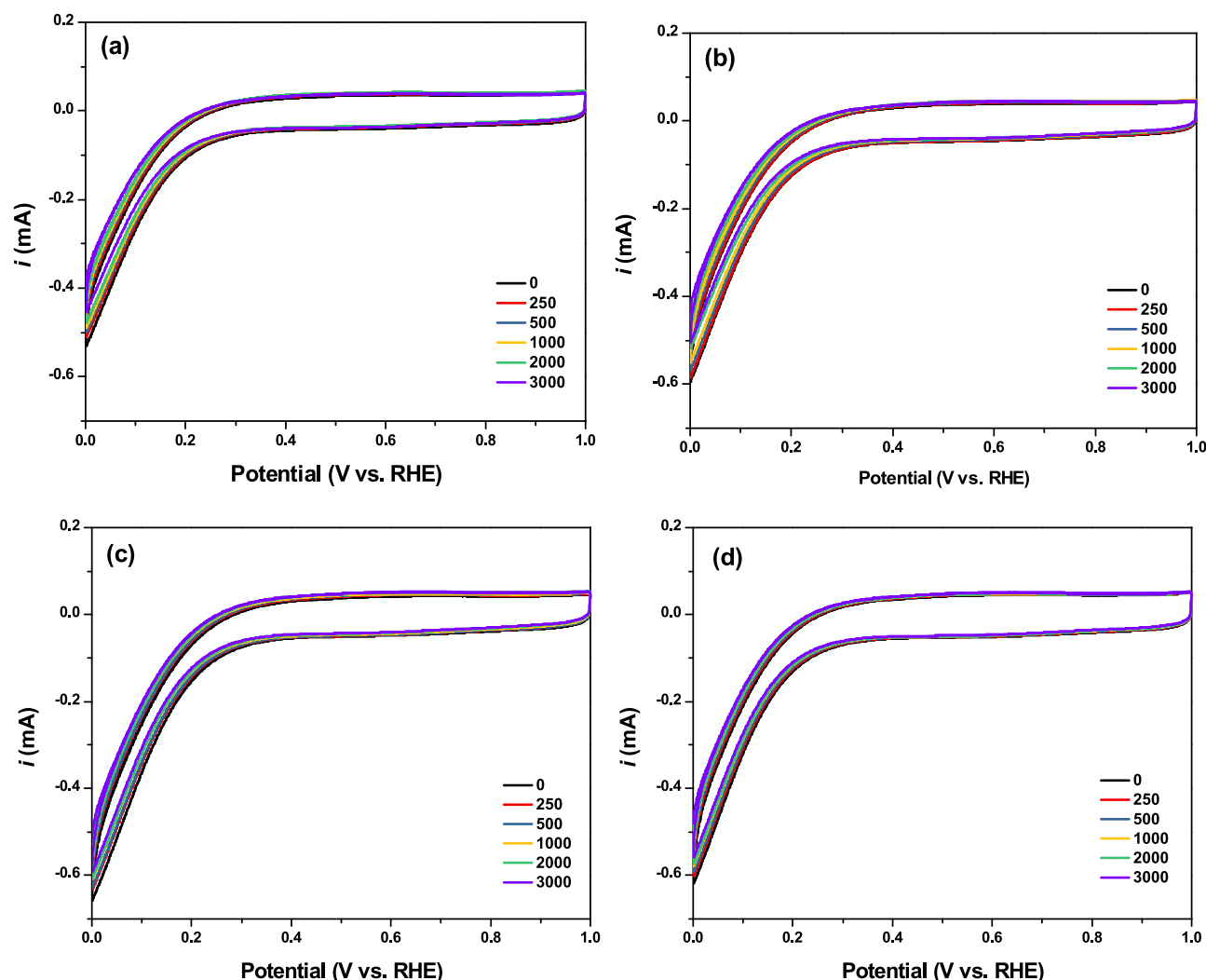


Fig. 4. Stability performance under accelerated durability testing (ADT) conditions in the O_2 -saturated 0.1 M $HClO_4$ electrolyte. (a) $p\text{-PDA}_1/\text{XC}$, (b) $p\text{-PDA}_2/\text{XC}$, (c) $p\text{-PDA}_5/\text{XC}$, and (d) $p\text{-PDA}_7/\text{XC}$. Reaction conditions: 40 μg of catalyst, and scan rate of 200 mV s^{-1} .

XC is more microporous with a higher S_{BET} of $276 \text{ m}^2 \text{ g}^{-1}$. The modification with $p\text{-PDA}$, as expected, resulted in the blocking of the micropores of XC and thus a drop in the S_{BET} and V_{pore} but an increase in the d_{pore} (Table 1). It was proposed that an electrocatalyst with a high S_{BET} could provide abundant catalytic sites and is thus beneficial for electrocatalytic reactions [32]. However, since XC with the highest S_{BET} is in general the least active and selective in 2e-ORR, the S_{BET} can be excluded as a key factor that determines the catalytic performance in the present case. Rather, the active sites generated by $p\text{-PDA}$ modification of XC are responsible for the enhanced activities of the $p\text{-PDA}/\text{XC}$ catalysts.

3.5. Elucidation of surface active sites

Since the carbon defects have been proposed as the active sites for the HPC-H24 [32] and MesoC catalysts [30] in 2e-ORR, the XC and $p\text{-PDA}/\text{XC}$ catalysts were subjected to Raman characterization. As shown in Fig. 9, there are two bands at 1320 cm^{-1} and 1585 cm^{-1} assignable to the D band and G band of the graphitic materials, respectively. The former is associated with the structural defects at the edge or on the basal plane, whereas the latter is relevant to graphitic carbon [32,41]. The intensity ratio of the D band to the G band ($I_{\text{D}}/I_{\text{G}}$) is an indication of the degree of disorder, which was calculated to be 0.95, 0.96, 0.94, 0.93, and 0.96 for the XC, $p\text{-PDA}_1/\text{XC}$, $p\text{-PDA}_2/\text{XC}$, $p\text{-PDA}_5/\text{XC}$, and $p\text{-PDA}_7/\text{XC}$ catalysts, respectively. The small

discrepancy in the $I_{\text{D}}/I_{\text{G}}$ ratios suggests that the abundance of the carbon defects or the size of the conjugated graphene units cannot account for the distinct difference in the catalytic performances among these catalysts, which is in line with the findings of Durante and co-workers [42] and Wang and co-workers [43]. Moreover, the $p\text{-PDA}_5/\text{XC}$ catalyst possessing the lowest $I_{\text{D}}/I_{\text{G}}$ ratio displayed the highest 2e-ORR activity, further excluding the possibility that the catalytic performance is dominated by the carbon defects for the $p\text{-PDA}/\text{XC}$ catalysts.

Fig. 10 presents the XPS spectra of the XC and $p\text{-PDA}/\text{XC}$ catalysts. The C 1s spectra in Fig. 10a were fitted into four peaks at BEs of ca. 284.6, 285.8, 287.0, and 288.9 eV assignable to graphitic C, C–N/C–O, C=O, and O–C=O, respectively [44]. The N 1s spectra (Fig. 10b) were fitted into three peaks, i.e., pyridinic N (398.6 eV), pyrrolic N (400.5 eV), graphitic N (401.6 eV) for all the $p\text{-PDA}/\text{XC}$ catalysts, in addition to a peak assignable to oxidic N (403.4 eV) for the $p\text{-PDA}_5/\text{XC}$ catalyst [11,25,40,41]. For the time being, we are unclear about the occurrence of the oxidic N species only on the $p\text{-PDA}_5/\text{XC}$ catalyst, though repetitive XPS measurements gave the same result. The oxidic N species has also been detected on some N-doped carbon materials and was not taken as the active sites for 2e-ORR to H_2O_2 in acidic medium [11,25,40]. For example, Li and co-workers fabricated nitrogen and oxygen co-doped ordered mesoporous carbon materials pyrolyzed at different temperatures. They identified that although O/N-OMC-900 possessed the highest content of the oxidized N species, it did not

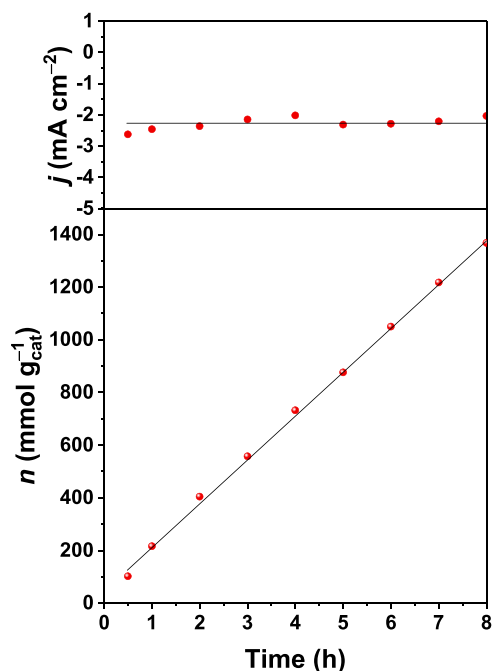


Fig. 5. The current density (top) and the photometrically determined H_2O_2 amount normalized by the catalyst mass (bottom) as a function of the reaction time. Reaction conditions: catalyst loading of $200 \mu\text{g cm}_{\text{geo}}^{-2}$, rotation speed of the working electrode of 1600 rpm, and the working voltage of 0.1 V vs. RHE. The 0.1 M HClO_4 electrolyte was continuously bubbled with O_2 .

show the best performance for the production of H_2O_2 among the electrocatalysts investigated [40]. As listed in Table S3, the total surface N content decreased steadily from the $p\text{-PDA}_1/\text{XC}$ catalyst to the $p\text{-PDA}_7/\text{XC}$ catalyst, which is anticipated from the change in the bulk N content (Table 1). The O 1 s spectra of the XC and $p\text{-PDA}/\text{XC}$ catalysts (Fig. 10c) were fitted into two peaks at 532.5 eV for $\text{C}=\text{O}$ and 533.9 eV for $\text{C}-\text{O}$ [44]. For the $p\text{-PDA}_1/\text{XC}$ and $p\text{-PDA}_2/\text{XC}$ catalyst, there is an additional O 1 s peak at lower BE of 531.1 eV, which is tentatively attributed to the occurrence of differential charging due to the presence of thicker $p\text{-PDA}$ coatings on these two catalysts.

Electrochemical capacitance measurements were used to determine the active surface areas of the $p\text{-PDA}/\text{XC}$ catalysts; the CV curves are presented in Fig. S5, and the corresponding plots of the average current density versus the scan rate are illustrated in Fig. 11. The ECSA value evolved in a volcanic curve, reaching a maximum at 2.82 mF cm^{-2} for the $p\text{-PDA}_5/\text{XC}$ catalyst, which is coincident with evolution of the H_2O_2 partial current at 0 V as compared in Fig. S6. Furthermore, the ECSA values plotted against the 2e-ORR activity showed a good linear relationship (Fig. S7). This correlation implies that 2e-ORR to H_2O_2 was catalyzed by active sites with similar nature on the $p\text{-PDA}/\text{XC}$ catalysts. And the difference in the 2e-ORR activity only lies in the difference in the abundance of the active sites.

As to the active sites on the carbon-based catalysts in the 2e-ORR to H_2O_2 reaction, Cui and co-workers reported that the carbon nanotubes with abundant $\text{C}-\text{O}$ and $\text{C}=\text{O}$ functional groups showed a significantly decreased overpotential and an enhanced selectivity up to $\sim 90\%$. By means of the density functional theory (DFT) calculations, they proposed that the carbon atoms next to the oxygen-containing functional groups are the active sites for ORR via the two-electron pathway [45]. Kim et al. identified that the sp^2 carbon atoms adjacent to the oxygen-containing functional groups are important ORR active sites, and the N dopant may affect the overall activity (and likely also the selectivity) by modifying the general chemical environment around the active sites [46]. Wang and co-workers identified that the OOH species, the key intermediate for O_2 reduction to H_2O_2 , prefers to adsorb on the C

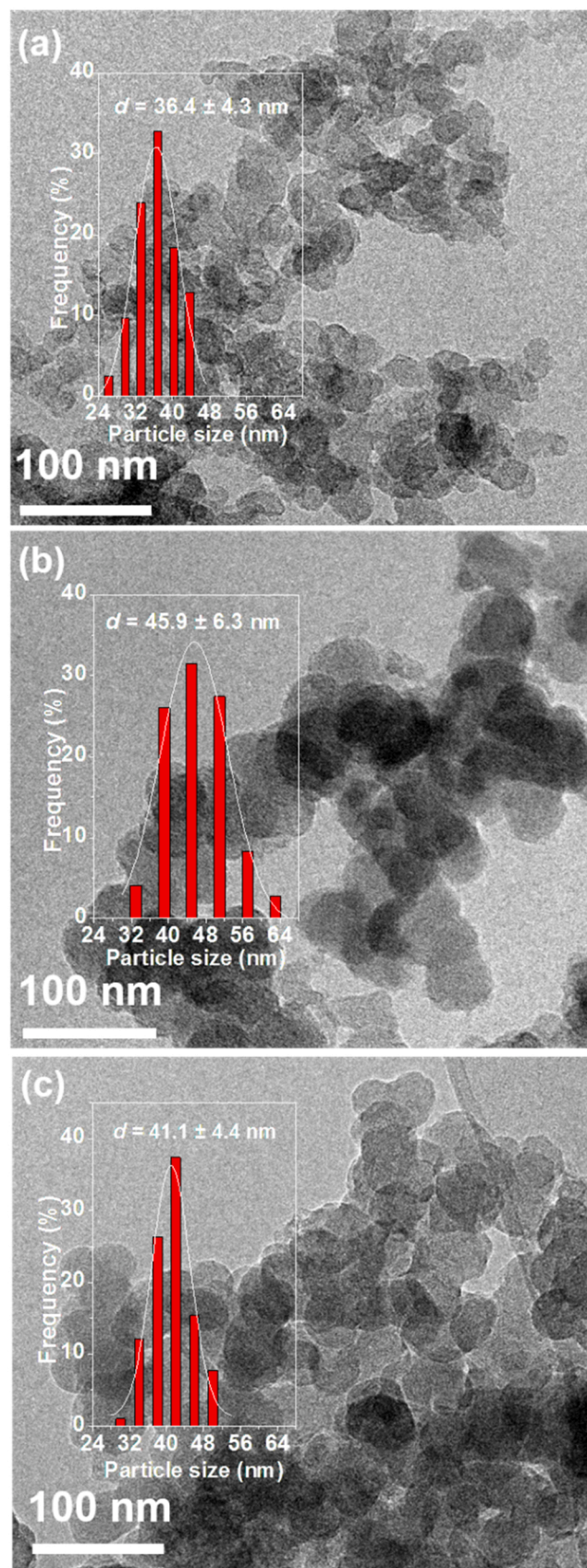
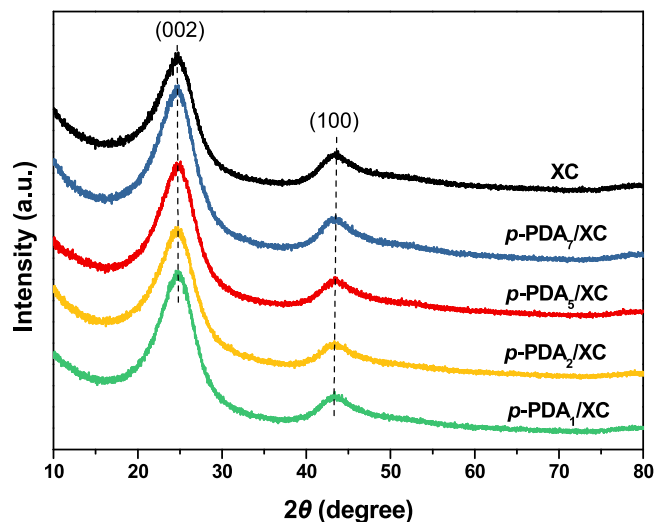
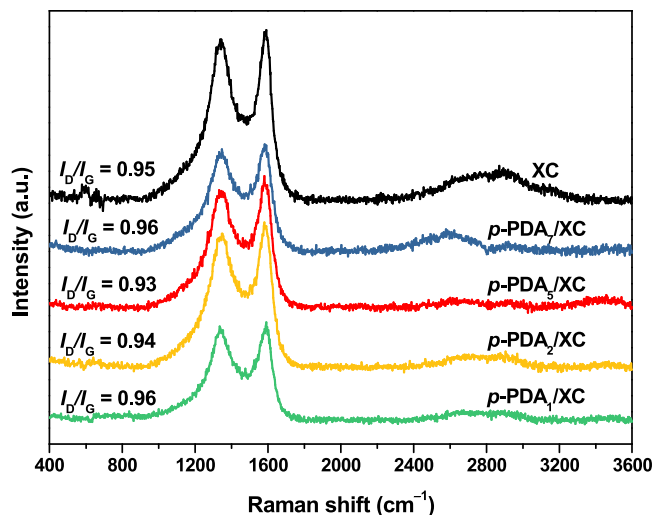
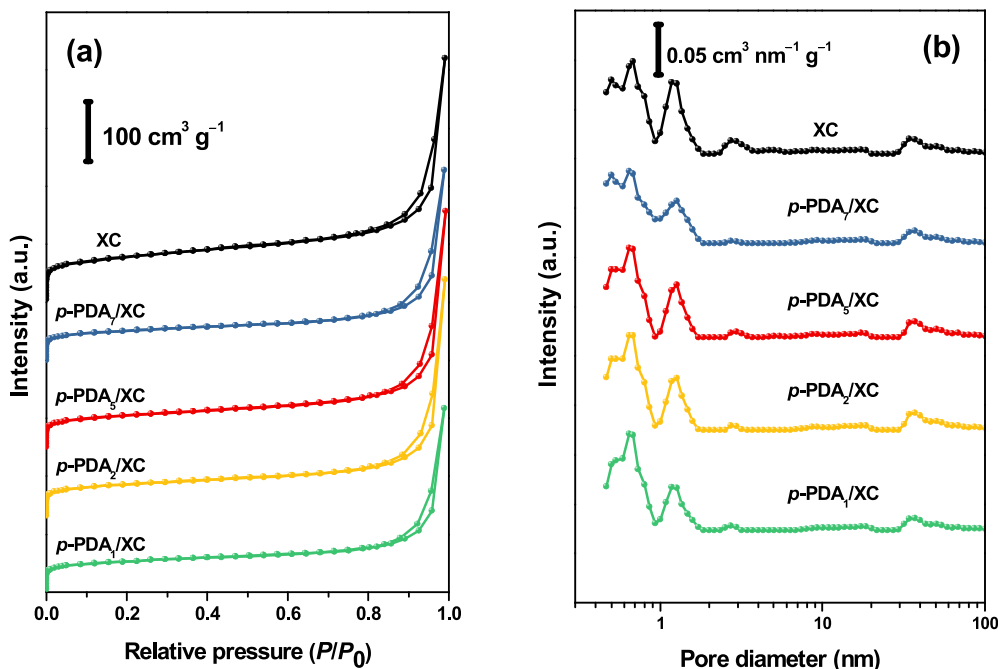


Fig. 6. TEM images and particle size distributions of the $p\text{-PDA}_5/\text{XC}$ catalyst at different synthetic stages. (a) XC, (b) PDA_5/XC , and (c) $p\text{-PDA}_5/\text{XC}$.

Table 1The bulk compositions and textural properties of the XC and *p*-PDA/XC catalysts.

Catalyst	Bulk composition (wt%)				S_{BET} (m ² g ⁻¹)	V_{pore} (cm ³ g ⁻¹)	d_{pore} (nm)
	C	H	O	N			
<i>p</i> -PDA ₁ /XC	95.38	0.413	2.977	1.23	188	0.44	5.02
<i>p</i> -PDA ₂ /XC	95.85	0.319	2.811	1.02	200	0.46	5.33
<i>p</i> -PDA ₅ /XC	95.69	0.358	3.042	0.91	209	0.59	5.26
<i>p</i> -PDA ₇ /XC	96.11	0.318	2.692	0.88	209	0.58	5.17
XC	97.11	0.216	2.674	/	276	0.59	4.97

Fig. 7. XRD patterns of the XC, *p*-PDA₁/XC, *p*-PDA₂/XC, *p*-PDA₅/XC, and *p*-PDA₇/XC catalysts.Fig. 9. Raman spectra of the XC and *p*-PDA/XC catalysts.Fig. 8. (a) N₂ adsorption–desorption isotherms and (b) pore size distributions of the XC and *p*-PDA/XC catalysts.

atom in vicinity to the N atom (C–N) on N-doped graphene. Nitrogen was also predicted to be more effective in lowering the overpotential than P and S [43]. Analogously, Anderson and co-workers attributed the higher catalytic activity of the nitrated Ketjenblack than the untreated carbon to the formation of carbon radical sites adjacent to substitutional N in graphite that are active in electroreduction of oxygen to H₂O₂ in acidic medium via an adsorbed OOH intermediate [47]. For an N-doped carbon catalyst, Nabaie and co-workers deduced that the C atoms adjacent to the N species (graphitic N, pyridinic N, and pyrrolic N) may be active for 2e-ORR rather than for 4e-ORR in acidic medium [48].

In light of these findings, we calculated the surface C–O/C–N and C=O contents on the basis of Fig. 10a; the results are summarized in Table 2. It turns out that the H₂O₂ partial current at 0 V positively correlates with the surface content of the C–O/C–N and C=O species (Fig. 12), substantiating that the C atoms in or adjacent to these species are the active sites for 2e-ORR to H₂O₂. Moreover, Wang and co-workers calculated the reaction barriers of the decisive steps for the 2e-ORR and

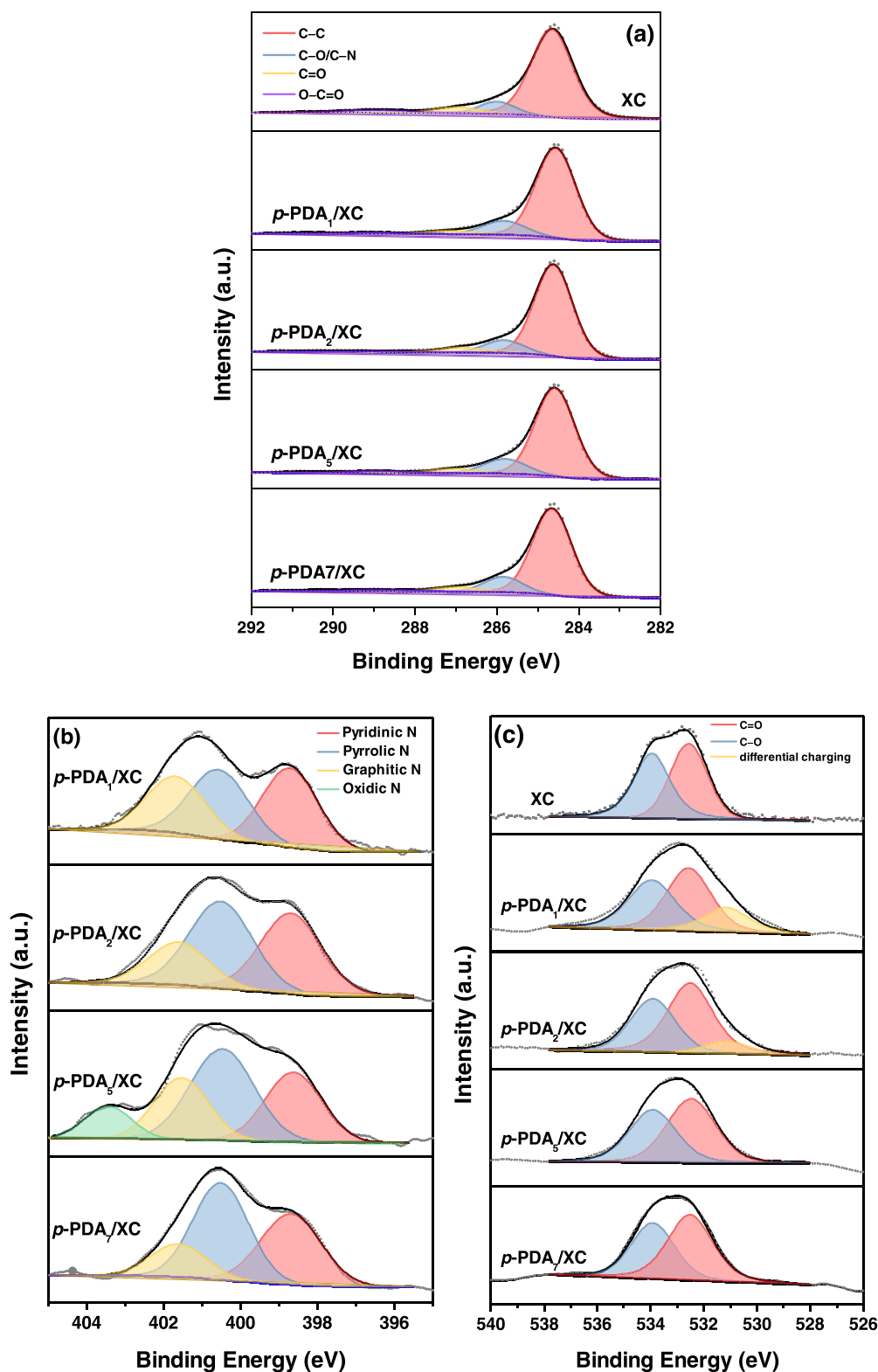


Fig. 10. (a) C 1s, (b) N 1s, and (c) O 1s spectra of the XC and *p*-PDA/XC catalysts.

4e-ORR pathways using molecular dynamics, and found that although the latter is thermodynamically more favorable, its reaction barrier is substantially higher than that of the former due to the large energy demand for the dissociation of the strong O–O bond [34]. Nabae and co-workers reached the same conclusion from a kinetic analysis of the reduction of O₂ over the N-doped carbon catalyst that the kinetic rate constant of the 2e-ORR pathway is substantially larger than that of the

4e-ORR pathway in acidic medium [48]. Therefore, the *p*-PDA/XC catalyst with a higher abundance of the active sites for the 2e-ORR pathway is anticipated to give a lower Tafel slope, which is nicely corroborated by the Tafel plots presented in Fig. 3. On the other hand, since the *p*-PDA₁/XC catalyst with the largest amount of *p*-PDA exhibited the lowest activity and selectivity to H₂O₂ among the *p*-PDA/XC catalysts, it is reasonable to deduce that the active sites formed at the

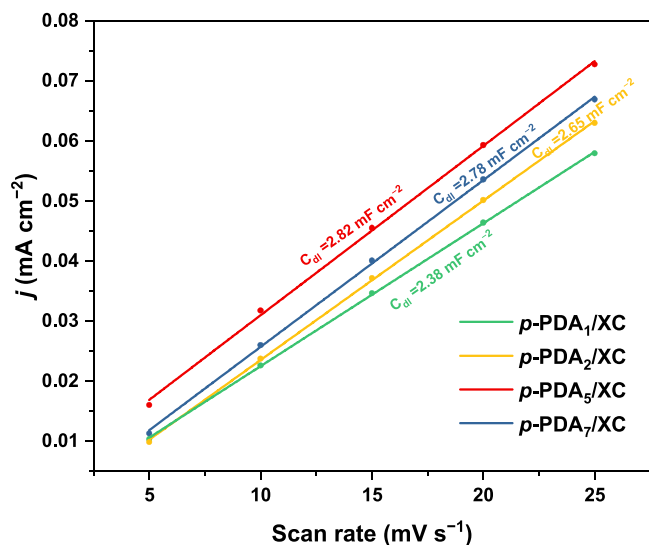


Fig. 11. Plot of the capacitive current density at 0.75 V against the scan rate for the *p*-PDA/XC catalysts.

Table 2

The C 1s fitting results of the XC and *p*-PDA/XC catalysts.

Catalyst	Surface C (at%)	Fraction in surface C				Surface C–O/N + C=O (at%)
		C–C	C–O/N	C=O	O–C=O	
<i>p</i> -PDA ₁ /XC	93.98	0.817	0.132	0.037	0.014	15.88
<i>p</i> -PDA ₂ /XC	94.26	0.816	0.113	0.060	0.011	16.31
<i>p</i> -PDA ₅ /XC	94.99	0.797	0.138	0.042	0.023	17.10
<i>p</i> -PDA ₇ /XC	93.32	0.797	0.133	0.045	0.025	16.61
XC	94.87	0.816	0.088	0.056	0.040	13.66

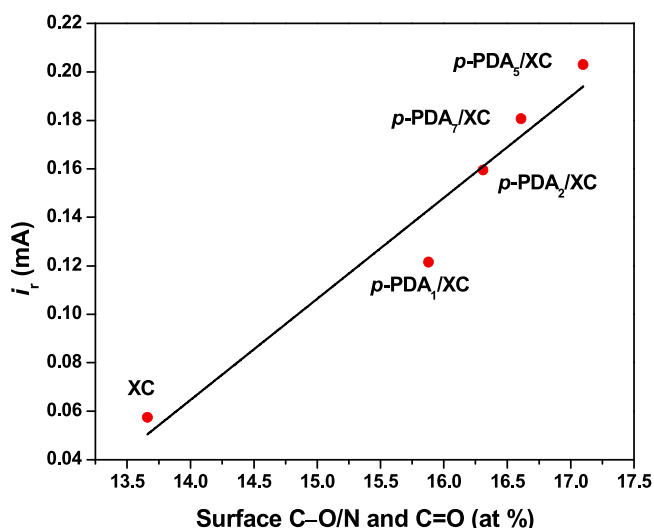


Fig. 12. Plot of the H₂O₂ partial current at 0 V vs. RHE as a function of the surface C–O/N and C=O content of the XC and *p*-PDA/XC catalysts.

interface between *p*-PDA and carbon black are more active and selective than the primary active sites on either *p*-PDA or carbon black. At the moderate amount of *p*-PDA, more interface sites are exposed, thus rendering the *p*-PDA₅/XC catalyst the best catalytic performance in

electroreduction of O₂ to H₂O₂.

4. Conclusion

We have successfully demonstrated a facile dopamine polymerization/coating–pyrolysis strategy for the synthesis of the *p*-PDA/XC electrocatalysts from inexpensive carbon and nitrogen precursors and benign preparation conditions. In the 2e-ORR to H₂O₂ reaction in acidic medium, the modification of *p*-PDA pronouncedly reduced the over-potential and enhanced the selectivity to H₂O₂. The *p*-PDA₅/XC catalyst with the optimal *p*-PDA loading exhibited the highest H₂O₂ selectivity of 96% and a stable H₂O₂ production rate of 171 mmol g_{cat}^{−1} h^{−1}, which are among the best results in the 2e-ORR reaction in acidic medium. The carbon atoms in or adjacent to the C–O/C–N and C=O species are proposed to be the highly active, selective, and stable active sites for electroreduction of O₂ to H₂O₂ in acid medium. Given the excellent catalytic performance and affordability of the *p*-PDA₅/XC catalyst, this study paves the way to the sustainable and safe production of H₂O₂ for many decentralized applications.

CRediT authorship contribution statement

Dan Wang: Investigation, Validation, Methodology, Writing – original draft, Formal analysis. **Sitan Li:** Investigation. **Xiaoxin Zhang:** Methodology, Project administration. **Bo Feng:** Investigation. **Yan Pei:** Investigation. **Yunfeng Zhu:** Methodology. **Qiang Xu:** Resources. **Zhen-Hua Li:** Validation. **Minghua Qiao:** Conceptualization, Formal analysis, Supervision, Writing – review & editing, Funding acquisition. **Baoning Zong:** Conceptualization, Writing – review & editing.

Declaration of Competing Interest

The authors declare that they have no known competing financial interests or personal relationships that could have appeared to influence the work reported in this paper.

Acknowledgements

This work was supported by the State Key Research and Development Project of China (2016YFB0301602), the State Key Laboratory of Catalytic Materials and Reaction Engineering (RIPP, SINOPEC), the National Natural Science Foundation of China (21872035), and the Science and Technology Commission of Shanghai Municipality (19DZ2270100).

Appendix A. Supporting information

Supplementary data associated with this article can be found in the online version at [doi:10.1016/j.apcatb.2021.121036](https://doi.org/10.1016/j.apcatb.2021.121036).

References

- [1] H.B. Li, B. Zheng, Z.Y. Pan, B.N. Zong, M.H. Qiao, *Front. Chem. Sci. Eng.* 12 (2018) 124–131.
- [2] S. Siahrostami, A. Verdaguier-Casadevall, M. Karamad, D. Deiana, P. Malacrida, B. Wickman, M. Escudero-Escribano, E.A. Paoli, R. Frydendal, T.W. Hansen, I. Chorkendorff, I.E.L. Stephens, J. Rossmeisl, *Nat. Mater.* 12 (2013) 1137–1143.
- [3] J.M. Campos-Martin, G. Blanco-Brieva, J.L.G. Fierro, *Angew. Chem. Int. Ed.* 45 (2006) 6962–6984.
- [4] S. Yang, A. Verdaguier-Casadevall, L. Arnarson, L. Silvio, V. Colic, R. Frydendal, J. Rossmeisl, I. Chorkendorff, I.E.L. Stephens, *ACS Catal.* 8 (2018) 4064–4081.
- [5] C. Xia, Y. Xia, P. Zhu, L. Fan, H.T. Wang, *Science* 366 (2019) 226.
- [6] J. Zhang, H. Zhang, M.J. Cheng, Q. Lu, *Small* 16 (2019), 1902845.
- [7] S. Yang, J. Kim, Y.J. Tak, A. Soon, H. Lee, *Angew. Chem. Int. Ed.* 55 (2016) 2058–2062.
- [8] Y.L. Wang, S.S. Li, X.H. Yang, G.Y. Xu, Z.C. Zhu, P. Chen, S.Q. Li, *J. Mater. Chem. A* 7 (2019) 21329–21337.
- [9] H. Zhao, X. Shen, Y. Chen, S.N. Zhang, P. Gao, X. Zhen, X.H. Li, G. Zhao, *Chem. Commun.* 55 (2019) 6173–6176.

- [10] E. Chen, M. Bevilacqua, C. Tavagnacco, T. Montini, C.M. Yang, P. Fornasiero, *Catal. Today* 356 (2019) 132–140.
- [11] Y. Sun, S. Li, Z.P. Jovanov, D. Bernsmeier, H. Wang, B. Paul, X. Wang, S. Kuehl, P. Strasser, *ChemSusChem* 11 (2018) 3388–3395.
- [12] Y.J. Sa, J.H. Kim, S.H. Joo, *Angew. Chem. Int. Ed.* 58 (2019) 1100–1105.
- [13] W. Zhou, X. Meng, J. Gao, A.N. Alshawabkeh, *Chemosphere* 225 (2019) 588–607.
- [14] X. Tian, X. Zhao, Y.Q. Su, L. Wang, H. Wang, D. Dang, B. Chi, H. Liu, E.J. M. Hensen, X.W. Lou, B.Y. Xia, *Science* 366 (2019) 850–856.
- [15] K. Gong, F. Du, Z. Xia, M. Durstock, L. Dai, *Science* 323 (2009) 760–764.
- [16] Y. Sun, I. Sinev, W. Ju, A. Bergmann, S. Dresch, S. Kuehl, C. Spoeer, H. Schmies, H. Wang, D. Bernsmeier, B. Paul, R. Schmack, R. Kraehnert, B. Roldan Cuenya, P. Strasser, *ACS Catal.* 8 (2018) 2844–2856.
- [17] Y. Jiang, P. Ni, C. Chen, Y. Lu, P. Yang, B. Kong, A. Fisher, X. Wang, *Adv. Energy Mater.* 8 (2018), 1801909.
- [18] M. Melchionna, P. Fornasiero, M. Prato, *Adv. Mater.* 31 (2019), 1802920.
- [19] N. Jia, T. Yang, S.F. Shi, X.B. Chen, Z.W. An, Y. Chen, S.W. Yin, P. Chen, A.C. S. Sustainable, *Chem. Eng.* 8 (2020) 2883–2891.
- [20] C.J. Shearer, A. Cherevan, D. Eder, *Adv. Mater.* 26 (2014) 2295–2318.
- [21] G.F. Han, F. Li, W. Zou, M. Karamad, J.P. Jeon, S.W. Kim, S.J. Kim, Y.F. Bu, Z.P. Fu, Y.L. Lu, S. Siahrostami, J.B. Baek, *Nat. Commun.* 11 (2020) 2209.
- [22] K.G. Qu, Y. Zheng, X.X. Zhang, K. Davey, S. Dai, S.Z. Qiao, *ACS Nano* 11 (2017) 7293–7300.
- [23] K. Dong, J. Liang, Y.Y. Wang, Z.Q. Xu, Q. Liu, Y.L. Luo, T.S. Li, L. Li, X.F. Shi, A. M. Asiri, Q. Li, D.W. Ma, X.P. Sun, *Angew. Chem. Int. Ed.* 60 (2021) 10583–10587.
- [24] H.W. Kim, M.B. Ross, N. Kornienko, L. Zhang, J.H. Guo, P.D. Yang, B.D. McCloskey, *Nat. Catal.* 1 (2018) 282–290.
- [25] T. Feller, F. Hasché, P. Strasser, M. Antonietti, *J. Am. Chem. Soc.* 134 (2012) 4072–4075.
- [26] J.L. Zhang, G.L. Chen, Q. Zhang, F. Kang, B. You, *ACS Appl. Mater. Interfaces* 7 (2015) 12760–12766.
- [27] K. Jiang, S. Back, A.J. Akey, C. Xia, Y. Hu, W. Liang, D. Schaak, E. Stavitski, J. K. Nørskov, S. Siahrostami, H.T. Wang, *Nat. Commun.* 10 (2019) 3997.
- [28] B.Q. Li, C.X. Zhao, J.N. Liu, Q. Zhang, *Adv. Mater.* 31 (2019), 1808173.
- [29] D.Q. He, L.J. Zhong, S.Y. Gan, J.X. Xie, W. Wang, Z.B. Liu, W. Guo, X. Yang, L. Niu, *Electrochim. Acta* 371 (2021), 137721.
- [30] S.C. Chen, Z.H. Chen, S. Siahrostami, T.R. Kim, D. Nordlund, D. Sokaras, S. Nowak, J.W.F. To, D. Higgins, R. Sinclair, J.K. Nørskov, T.F. Jaramillo, Z.N. Bao, *ACS Sustain. Chem. Eng.* 6 (2018) 311–317.
- [31] J.J. Gao, H.B. Yang, X. Huang, S.F. Hung, W.Z. Cai, C.M. Jia, S. Miao, H.M. Chen, X.F. Yang, Y.Q. Huang, T. Zhang, B. Liu, *Chem* 6 (2020) 658–674.
- [32] Y. Liu, X. Quan, X. Fan, H. Wang, S. Chen, *Angew. Chem. Int. Ed.* 54 (2015) 6837–6841.
- [33] V. Perazzolo, G. Daniel, R. Brandiele, L. Picelli, G.A. Rizzi, A.A. Isse, C. Durante, *Chem. Eur. J.* 27 (2021) 1002–1014.
- [34] K. Zhao, Y. Su, X. Quan, Y.M. Liu, S. Chen, H.T. Yu, *J. Catal.* 357 (2018) 118–126.
- [35] H. Lee, B.P. Lee, P.B. Messersmith, *Nature* 448 (2007) 338–341.
- [36] D. Iglesias, A. Giuliani, M. Melchionna, S. Marchesan, A. Criado, L. Nasi, M. Bevilacqua, C. Tavagnacco, F. Vizza, M. Prato, P. Fornasiero, *Chem* 4 (2018) 106–123.
- [37] R. Arrigo, M. Havecker, S. Wrabetz, R. Blume, M. Lerch, J. McGregor, E.P. J. Parrott, J.A. Zeitler, L.F. Gladden, A. Knop-Gericke, R. Schlögl, D.S. Su, *J. Am. Chem. Soc.* 132 (2010) 9616–9630.
- [38] K. Jiang, J.J. Zhao, H.T. Wang, *Adv. Func. Mater.* 30 (2020), 2003321.
- [39] S.C. Chen, Z.H. Chen, S. Siahrostami, D. Higgins, D. Nordlund, D. Sokaras, T. R. Kim, Y.Z. Liu, X.Z. Yan, E. Nilsson, R. Sinclair, J.K. Nørskov, T.F. Jaramillo, Z. N. Bao, *J. Am. Chem. Soc.* 140 (2018) 7851–7859.
- [40] M.C. Qin, S.Y. Fan, L. Wang, G.Q. Gan, X.Y. Wang, J. Cheng, Z.P. Hao, X.Y. Li, *J. Colloid Interface Sci.* 562 (2020) 540–549.
- [41] J. Park, Y. Nabae, T. Hayakawa, M.A. Kakimoto, *ACS Catal.* 4 (2014) 3749–3754.
- [42] V. Perazzolo, C. Durante, R. Pilot, A. Paduano, J. Zheng, G.A. Rizzi, A. Martucci, G. Granozzi, A. Gennaro, *Carbon* 95 (2015) 949–963.
- [43] Y. Xia, X.H. Zhao, C. Xia, Z.Y. Wu, P. Zhu, J.Y. Kim, X.W. Bai, G.H. Gao, Y.F. Hu, J. Zhong, Y.Y. Liu, H.T. Wang, *Nat. Commun.* 12 (2021) 4225.
- [44] T.N. Pham-Truong, T. Petenzi, C. Ranjan, H. Randriamahazaka, J. Ghilane, *Carbon* 130 (2018) 544–552.
- [45] Z. Lu, G. Chen, S. Siahrostami, Z. Chen, K. Liu, J. Xie, L. Liao, T. Wu, D. Lin, Y. Liu, T.F. Jaramillo, J.K. Nørskov, Y. Cui, *Nat. Catal.* 1 (2018) 156–162.
- [46] H.W. Kim, V.J. Bukas, H. Park, K.M. Diederichsen, J. Lim, Y.H. Cho, J. Kim, W. Kim, T.H. Han, J. Voss, A.C. Luntz, B.D. McCloskey, *ACS Catal.* 10 (2020) 852–863.
- [47] R.A. Sidik, A.B. Anderson, N.P. Subramanian, S.P. Kumaraguru, B.N. Popov, *J. Phys. Chem. B* 110 (2006) 1787–1793.
- [48] Y. Wu, A. Muthukrishnan, S. Nagata, Y. Nabae, *J. Phys. Chem. C* 123 (2019) 4590–4596.